Femtosecond photoelectron spectroscopy of $I_2^-(Ar)_n$ clusters ($n=6,9,12,16,20$)

B. Jefferys Greenblatt,[a] Martin T. Zanni, and Daniel M. Neumark
Department of Chemistry, University of California, Berkeley, California 94720 and Chemical Sciences Division, Lawrence Berkeley National Laboratory, Berkeley, California 94720

(Received 15 July 1999; accepted 9 September 1999)

The photodissociation of I_2^- embedded in mass-selected $I_2^-(Ar)_n$ clusters ($n=6-20$) was studied using femtosecond photoelectron spectroscopy. The $\tilde{A}'\leftarrow\tilde{X}$ transition in the I_2^- chromophore was excited using a femtosecond pump pulse, and the subsequent dynamics were followed by photodetachment with a femtosecond probe pulse and measurement of the resulting photoelectron spectrum. In all clusters, dissociation of the I_2^- is complete by 300 fs. From 300 fs to 1 ps, the spectra yield the number of Ar atoms interacting with the I^- fragment. At later times, recombination of I_2^- occurs in $I_2^-(Ar)_{n\geqslant 12}$ on both the $\tilde{X}$ and $\tilde{A}$ states. Analysis of the spectra yields the time scale for $\tilde{X}$ state vibrational relaxation and solvent evaporation. In $I_2^-(Ar)_{20}$, energy transfer from I_2^- to Ar atoms through vibrational relaxation is slightly faster than energy loss from the cluster through Ar evaporation, indicating the temporary storage of energy within Ar cluster modes. © *1999 American Institute of Physics.* [S0021-9606(99)01245-3]

I. INTRODUCTION

The photodissociation I_2^- in small, mass-selected clusters provides an unprecedented opportunity to study the effects of solvation on an elementary chemical reaction. The pioneering work by the Lineberger group on $Br_2^-(CO_2)_n$ and $I_2^-(CO_2)_n$ photodissociation[1,2] laid the foundation for further experiments in these and related systems,[3–5] including $I_2^-(Ar)_n$ clusters,[6,7] femtosecond pump–probe experiments,[2,4,8–13] and the photodissociation of I_2^- in solution.[14–18] Considerable theoretical work has also been performed on these systems.[19–32] The general picture which has emerged is that ''caging'' of photodissociated I_2^- and other dihalides can occur in clusters with less than one full solvent shell, producing recombined (I_2^--based) products. The caging fraction and recombination rate depend strongly on the number and identity of the solvating species. However, an understanding of the complex dynamics that occur in these clusters is far from complete.

In this paper we use anion femtosecond photoelectron spectroscopy (FPES),[33] a time-resolved, pump–probe experiment, to investigate $I_2^-(Ar)_n$ clusters. In this experiment, the $\tilde{A}'\leftarrow\tilde{X}$ transition in the I_2^- chromophore (Fig. 1) is excited by a femtosecond pump pulse centered at 780 nm. The resulting wavepacket evolves on this excited potential surface, leading to direct dissociation as well as nonadiabatic transitions to other electronic states with possible recombination of fragments. A second, delayed femtosecond probe pulse detaches an electron from the anion, and the photoelectron spectrum is measured. Since the electron kinetic energy depends on the difference between anion and neutral potential energies, quantitative identification of electronic and vibrational states of the anion is possible when the neutral potential energy surfaces are well-characterized. The strength of the technique lies in its ability to follow the wave packet dynamics along the entire reaction coordinate on multiple electronic states, without changing the probe wavelength.

$I_2^-(Ar)_n$ clusters represent a weakly interacting system, as the I_2^-–Ar well depth (53 meV) is much smaller than that of the I_2^- $\tilde{X}$ state (1.014 eV).[34] Despite the small interaction with each solvent atom, the collective effect of many solvent atoms has a strong influence on the photodissociation dynamics. We previously reported FPE spectra of $I_2^-(Ar)_6$ and $I_2^-(Ar)_{20}$ clusters,[12] for which the caging fractions are 0% and 100%, respectively.[7] This earlier work provided information on the interaction time of the solvent with dissociating I^-, and time scales for electronic transitions and subsequent vibrational relaxation of I_2^-. Here we consider these clusters in more detail and three additional intermediate-sized clusters, yielding a fuller picture of how the dissociation, recombination, and relaxation dynamics evolve with cluster size. A forthcoming paper details results for $I_2^-(CO_2)_n$ clusters over a similar range of sizes.[35]

A summary of prior work on $I_2^-(Ar)_n$ clusters is essential to understanding the FPES results. Vorsa *et al.*[6,7] excited the $\tilde{A}'\leftarrow\tilde{X}$ transition in mass-selected clusters with a single laser pulse at 790 nm and measured the photofragment masses. They observed only $I^-(Ar)_m$ fragments from clusters with $n<10$, slowly being replaced by $I_2^-(Ar)_m$ as n increases with the $I^-(Ar)_m$ channel vanishing by $n=17$. The numbers of Ar atoms present in both $I^-(Ar)_m$ and $I_2^-(Ar)_m$ fragments were smaller than that of the parent cluster, with more atoms lost in the I_2^- fragments. This observation was consistent with the expectation that the available energy in the cluster is dissipated through Ar evaporation. Interestingly, two distinct $I_2^-(Ar)_m$ fragment size groupings were observed. It was suggested that these corresponded to I_2^- $\tilde{X}$ and $\tilde{A}$ state products, a hypothesis confirmed by our subsequent FPES study[12] and

[a]Current address: NASA Ames Research Center, Atmospheric Chemistry and Dynamics Branch, Mail Stop 245-5, Moffett Field, California 94035.

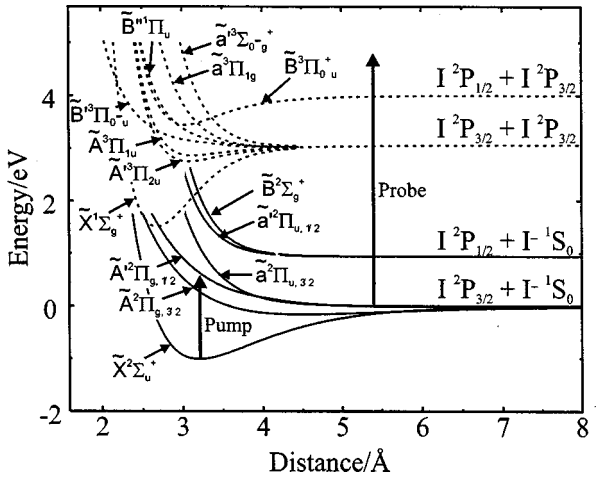

FIG. 1. Potential energy curves for bare I_2^-. Solid lines, I_2^-. Dotted lines, I_2.

molecular dynamics simulations.[25,28,36] Two $I^-(Ar)_m$ fragment groupings were also observed from larger ($n \geqslant 11$) clusters, for which no explanation was given, but Faeder *et al.*[25] later attributed the high-mass channel to dissociation on the $\tilde{X}$ or $\tilde{A}$ state, rather than the initially excited $\tilde{A}'$ state.

Vorsa *et al.*[11] also performed a time-resolved absorption recovery experiment on $I_2^-(Ar)_{20}$ in which these clusters were excited with a fs-duration pulse at 790 nm, then re-excited with a second, identical pulse after a variable time delay. The total flux of two-photon photofragments was recorded, a signature of I_2^- absorption near the bottom of the $\tilde{X}$ state well. This absorption was found to recover with an exponential time constant $t_{1/e}$ of 127 ps.

Our initial FPES studies on $I_2^-(Ar)_6$ and $I_2^-(Ar)_{20}$ clusters[12] also involved excitation of I_2^- to the dissociative $\tilde{A}'$ state. In $I_2^-(Ar)_6$, $I^-(Ar)_{n\approx 1}$ was observed to leave the cluster in ~1.2 ps. In $I_2^-(Ar)_{20}$, caging by the solvent resulted in recombination and vibrational relaxation of I_2^- on both the $\tilde{X}$ and $\tilde{A}$ states; these processes were complete in ~200 ps and ~35 ps, respectively. More recently, FPES was used to detect resonant stimulated impulsive Raman scattering in the ground electronic state of several $I_2^-(Ar)_n$ clusters, yielding the I_2^- vibrational frequency as a function of cluster size.[37] Finally, conventional photoelectron spectra have been measured for $I_2^-(Ar)_n$ clusters with up to 20 Ar atoms in order to further characterize the solvation energetics of these species.[38]

Minimum energy structures of $I_2^-(Ar)_n$ clusters have been calculated by Faeder *et al.*[25] and Batista *et al.*[24,39] The first 6 Ar atoms surround the I_2^- axis in a ring configuration, with the next 7 Ar atoms solvating one I atom, and any additional atoms cluster to the other I atom, completing a full shell at $n=20$. Asymmetrically-solvated clusters have an excess negative charge on the more solvated I atom. Figure 2 shows calculated structures for three cluster sizes; $n=6$, 12, and 20.

Maslen *et al.*[21] investigated the effect of solvent on charge localization in different I_2^- electronic states. In the $\tilde{X}$ and $\tilde{A}$ states (see Fig. 1), excess negative charge is associated with the more solvated atom, localizing completely at sufficiently large internuclear distances. In the $\tilde{A}'$ state, however, the polarizability of the molecule is negative along the I_2^- axis,[25] so that the charge tends to localize on the less solvated atom. The ($\tilde{X}$,$\tilde{A}$) and $\tilde{A}'$ states are termed normal and anomalous charge-switching states, respectively. When I_2^- is excited by the pump pulse, the lowest energy solvent configuration on the $\tilde{X}$ state becomes energetically unfavorable on the $\tilde{A}'$ state. This results in motion of the solvent atoms back toward the charge. However, the solvent atoms are unable to completely surround the charge, because it is always localized on the less solvated I atom, resulting in a symmetric solvent distribution as the minimum energy structure in this state. As the I_2^- bond lengthens, the likelihood of an electronic transition to the $\tilde{X}$ or $\tilde{A}$ state increases; when this occurs, the solvent atoms will rearrange into a more heavily solvated configuration around the I^-, similar to the starting arrangement. These charge localization effects are expected to play a major role in the dynamics subsequent to photoexcitation.

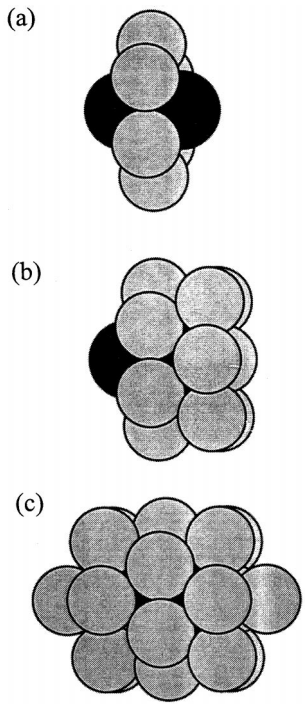

FIG. 2. Calculated minimum-energy structures (Refs. 25, 39) of selected $I_2^-(Ar)_n$ clusters: (a) $I_2^-(Ar)_6$; (b) $I_2^-(Ar)_{12}$; (c) $I_2^-(Ar)_{20}$.

Time-resolved dynamics of $I_2^-(Ar)_n$ clusters were investigated by Faeder *et al.*,[25,28] and Batista and Coker[24] with molecular dynamics (MD) simulations, using a surface-hopping algorithm to model electronic transitions. In both sets of studies, the MD results were compared to the caging fractions and product mass distributions measured by Vorsa *et al.*[7,11] Many of the experimental features were at least qualitatively reproduced by the simulations, including the bimodal $I_2^-(Ar)_m$ photofragment distribution resulting from excited state recombination. In addition, the latter study by Faeder *et al.*[28] simulated the transient photoelectron spectra of $I_2^-(Ar)_6$ and $I_2^-(Ar)_{20}$ to allow comparison with FPE spectra of Greenblatt *et al.*[12]

The simulations predict that I^- and I fragments separate by as much as 8–15 Å during the first 1–2 ps.[24] In the larger clusters $[I_2^-(Ar)_{n\geq 9}]$, attractive interactions with the solvent atoms prevent the fragments from leaving the cluster for some trajectories, leading to transitions to the $\tilde{X}$ or $\tilde{A}$ states which usually result in I_2^- recombination and vibrational relaxation. For $I_2^-(Ar)_{20}$, recombination on the $\tilde{X}$ state occurs in 5–10 ps, with vibrational relaxation requiring more than 200 ps to complete.[25,28] The number of solvent atoms lost to evaporation slightly lags the solute internal energy. Recombination on the $\tilde{A}$ state takes up to 40 ps, but relaxation is much more rapid (~10 ps), owing to the smaller amount (~10%) of internal energy required to be dissipated. However, the solvent evaporation rate is slow, presumably because even complete vibrational relaxation of the $\tilde{A}$ state releases only ~0.1 eV into a large number of solvent atoms, leading to a significant lag time between relaxation and evaporation.

The goal of this study, as well as the forthcoming study of $I_2^-(CO_2)_n$ clusters,[35] was to use FPES to observe how the dynamics evolve from the uncaged to caged cluster size limits. Key findings for $I_2^-(Ar)_n$ clusters include: (1) Determination of the initial solvent configuration from measuring the number of solvent atoms around I^- at early time delays (~300 fs), confirming the prediction of anomalous charge-switching in the $\tilde{A}'$ state. (2) Measurement of the time-resolved number of solvent atoms in both the I^- and I_2^- $\tilde{X}$ state channels, providing information on relaxation dynamics from the point of view of solvent evaporation. (3) A detailed picture of the vibrational relaxation in caged photofragments, especially $I_2^-(Ar)_{20}$, which relaxes almost completely over a ~200 ps time scale. (4) Unambiguous identification of recombination, relaxation, and solvent evaporation on the I_2^- $\tilde{A}$ state in several clusters.

II. EXPERIMENT

The experimental apparatus has been described in detail elsewhere[13] and will only be summarized briefly here. To generate cluster anions, Ar carrier gas (20 psig) is passed over solid I_2 and expanded into vacuum through a piezoelectric pulsed valve running at a repetition rate of 500 Hz. A 1.5 keV electron gun crosses the resulting supersonic expansion, creating vibrationally cold negative ions, which are then pulse-extracted into a Wiley–McLaren[40] time-of-flight mass spectrometer and accelerated to 0.7–1.8 keV. Femtosecond pump (780 nm, 80 fs, 150 μJ) and probe (260 nm, 100 fs, 20 μJ) pulses, produced from a Clark-MXR regeneratively amplified Ti:sapphire laser, intersect the ions at the focus of a magnetic bottle electron spectrometer,[41] resulting in excitation and photodetachment of the ions. Electron kinetic energies (eKE) for the resulting photoelectrons are measured by time-of-flight. High collection efficiency of the magnetic bottle enables rapid acquisition (400–1200 s) of photoelectron spectra. Since the probe photon has sufficient energy to detach electrons from the ground state of $I_2^-(Ar)_n$ clusters, spectra are not background-free, so a fraction of this ''probe only'' spectrum was subtracted from the pump–probe spectra in order to facilitate observation of the two-photon signals.

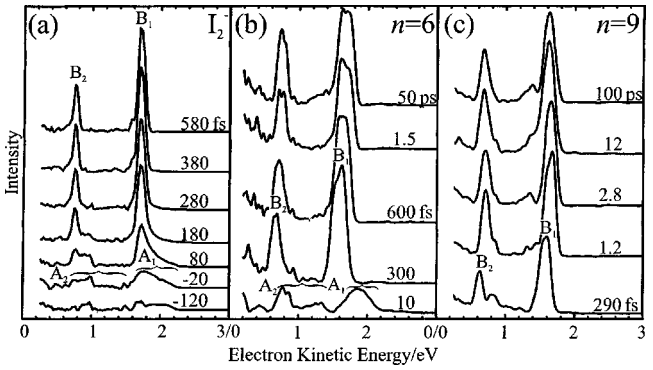

FIG. 3. FPE spectra at selected time delays: (a) I_2^-; (b) $I_2^-(Ar)_6$; (c) $I_2^-(Ar)_9$. Pump photon energy = 1.589 eV, probe photon energy = 4.768 eV.

The energy resolution of the I_2^- photoelectron spectrum has been improved ~4× using pulsed deceleration[42] of the anions just prior to laser interaction. This technique, recently added to the spectrometer, was only employed for bare I_2^-. However, since the resolution scales as $(EU/m)^{1/2}$, where E is the electron kinetic energy, U is the anion kinetic energy, and m is the anion mass,[33] the behavier $I_2^-(Ar)_n$ clusters have inherently narrower resolution, and light clusters were measured at slower beam energies (~650 eV) to improve their resolution. Typical resolution for 1 eV electrons was 90 meV for I_2^-, and 90–190 meV for $I_2^-(Ar)_n$ clusters.

III. RESULTS

Time-resolved photoelectron spectra have been measured for I_2^- and for $I_2^-(Ar)_n$ clusters with $n=6$, 9, 12, 16, and 20. Each molecule was studied at multiple pump–probe time delays, with a maximum time delay ranging from 50 to 200 ps. In addition, the $I_2^-(Ar)_{20}$ cluster was measured at 3 ns pump–probe delay. Spectra at selected time delays, representing only a fraction of the total data set,[43] are shown in Figs. 3 and 4. Features are labeled with capital letter designations, following a scheme summarized in Table I; these assignments are based on our past FPES studies[12,33] of I_2^-

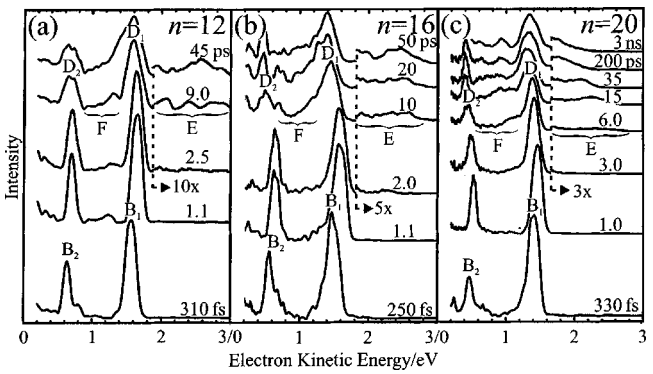

FIG. 4. FPE spectra at selected time delays: (a) $I_2^-(Ar)_{12}$; (b) $I_2^-(Ar)_{16}$; (c) $I_2^-(Ar)_{20}$. Pump photon energy = 1.589 eV, probe photon energy = 4.768 eV.

TABLE I. Labeling system of features observed in FPES, with corresponding assignments. A_1 and A_2 refer to transitions to the I atom in its $^2P_{3/2}$ and $^2P_{1/2}$ states, respectively (same for *B*, *D*).

Label	Assignment
A_1, A_2	$I_2 \leftarrow I_2^- \tilde{A}'$ (short-time transient)
B_1, B_2	$I \leftarrow I^-$
D_1, D_2	$I_2 \leftarrow I_2^- \tilde{A}$
E	$I_2 \tilde{X} \leftarrow I_2^- \tilde{X}$ inner turning point (ITP)
F	$I_2 \tilde{X} \leftarrow I_2^- \tilde{X}$ outer turning point (OTP)
	$I_2^* \leftarrow I_2^- \tilde{X}$

and $I_2^-(Ar)_{6,20}$ and the simulations by Faeder *et al.*[28] Further comment on these assignments is presented in the Analysis and Discussion. In considering the spectra below, recall that the caging fraction is 0 for $n \leqslant 9$, 0.46 for $n=12$, 0.98 for $n=16$, and 1.00 for $n=20$.[7]

Bare I_2^- displays two broad features A_1 (1.7–2.2 eV) and A_2 (0.8–1.3 eV) peaking near 0 fs, and transforming into sharper features B_1 (1.71 eV) and B_2 (770 meV) which reach their full height by ~280 fs. As discussed previously, the *A* features are transients from dissociating I_2^- on the $\tilde{A}'$ state (see Fig. 1).[33,44] Features B_1 and B_2, differing in energy by the spin–orbit splitting of neutral I (943 meV),[45] correspond to fully dissociated I^-.

In $I_2^-(Ar)_6$, the spectrum initially resembles bare I_2^-, displaying *A* features at 10 fs which evolve to *B* features by 300 fs. B_1 and B_2 are shifted 120 meV to lower eKE relative to bare I^-. This shift is due to the presence of Ar atoms, since the $I^- - Ar$ bond is stronger than that of I–Ar, resulting in an increase in electron affinity.[46] Between 300 fs and 1.5 ps, the energies of the *B* features increase 80 meV. This is attributed to a net decreased interaction between the Ar atoms and I^- as dissociation progresses and $I^-(Ar)_m$ fragments form (with $\langle m \rangle \cong 1$, see Discussion).[12,28] Through 200 ps there is an additional eKE increase of 10 meV, due to Ar atom evaporation from the $I^-(Ar)_m$ fragment.

A similar evolution of features *A* to *B* occurs in all the larger clusters during the first 300 fs and is therefore not shown. In the $I_2^-(Ar)_9$ FPE spectra, the *B* features appear 150 meV lower than bare I^-, and from 300 fs to 1.1 ps the eKE of these peaks increase by 80 meV, as for $I_2^-(Ar)_6$. However, from 2.8 to 12 ps, the features decrease 30 meV in energy. This is interpreted to indicate increased solvation of the I^- atom, the cause for which will be explored in the Discussion. Through 100 ps, the energy increases again by 10 meV, due to Ar atom evaporation.

In the $I_2^-(Ar)_{12}$ cluster, the smallest studied here for which caging occurs, the *B* features closely track those in $I_2^-(Ar)_9$ from 310 fs through 2.5 ps, after which they broaden significantly toward lower eKE, and decrease ~25% in integrated intensity. At this point (9.0 ps), the features are relabeled D_1 and D_2. The broadening and decrease in intensity are attributed to recombination on the I_2^- $\tilde{A}$ and $\tilde{X}$ states, respectively (see Discussion). Between 2.5 and 9.0 ps, feature *E* appears between 1.9 and 3.0 eV, along with a broad feature *F* between 900 meV and 1.3 eV. These features are assigned to vibrationally excited I_2^- on the $\tilde{X}$ state. Both features *E* and *F* become more prominent out to 45 ps.

Similar to $n=12$, the $I_2^-(Ar)_{16}$ spectra display *B* features initially 220 meV lower than I^-, increasing by 90 meV through 1.1 ps. Between 2.0 and 20 ps, the features broaden and shift to lower eKE by 240 meV, where they are relabeled D_1 and D_2, due to recombination on the $\tilde{A}$ state. Between 2.0 and 10 ps, features $E(1.7–2.9\,\text{eV})$ and $F(0.8–1.3\,\text{eV})$ grow in, more intense relative to the *D* features than in $I_2^-(Ar)_{12}$, due to recombination on the I_2^- $\tilde{X}$ state. Between 10 and 50 ps, the high-energy edge of feature *E* shifts ~100 meV to lower energy, indicating partial vibrational relaxation.

In the $I_2^-(Ar)_{20}$ FPE spectra, the *B* features appear 300 meV lower eKE than I^- and increase by 50 meV through 1.0 ps. After this time delay, they reverse direction and are relabeled D_1 and D_2, shifting 140 meV to lower eKE through 30 ps due to $\tilde{A}$ state recombination; this is accompanied by broadening and a ~40% decrease in integrated intensity. Features $E(1.6–2.7\,\text{eV})$ and $F(0.5–1.2\,\text{eV})$ appear by 6.0 ps. The high-energy edge of feature *E* shifts ~700 meV to lower eKE through 3 ns, while feature *F* undergoes a complex evolution in structure. The changes in features *E* and *F* are due to extensive $\tilde{X}$ state vibrational relaxation.

IV. ANALYSIS

The goal in simulating the FPE spectra is to determine, at each time delay, the state of the cluster. We do this by evaluating and simulating the possible contributions to a FPE spectrum, and then determining which combination of these various components gives the best fit to a particular FPE spectrum. For each spectrum, we seek to answer the following: (1) Have I and I^- recombined? (2) If I^- is present, how many solvent atoms surround it? (3) If I_2^- is present, what is the electronic and vibrational state, and how many solvent atoms surround it? (4) What are the relative populations of the different states (I_2^- $\tilde{X}$, I_2^- $\tilde{A}$, I^-) in the cluster? To answer these questions one must be able to simulate the contributions of solvated I^- and solvated I_2^- in its various vibrational and electronic states. In this section we discuss the methodology for doing this.

A. Solvated I^-

It was assumed that, after the initial (~ 300 fs) I_2^- dissociation, I and I^- are well-separated, so that I has little influence on the photoelectron spectrum of I^-. This is substantiated by the observation that pairs of features (B_1 and B_2) are present in all spectra at short times (<1–2 ps), differing in energy by approximately the spin–orbit splitting of I (943 meV) which is characteristic of the photoelectron spectrum of I^- though shifted to lower eKE. The shift is a well-understood effect, arising from the difference in binding energy between the $I^- - Ar$ (45.8 meV) and I–Ar (18.8 meV) bonds.[46] These differences have been measured precisely using zero electron kinetic energy (ZEKE) and partially-discriminated threshold photodetachment spectroscopy of $I^-(Ar)_n$ clusters.[46]

At all times, one can then determine $\langle n_{I^-} \rangle$, the average number of Ar atoms surrounding the I^-, by comparing the

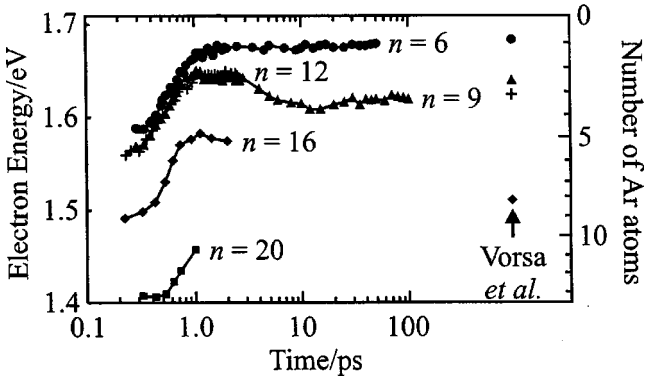

FIG. 5. Center eKE of feature B_1 vs time, for all $I_2^-(Ar)_n$ clusters. Number of Ar atoms ($\langle n_1^- \rangle$) is shown on righthand axis, as determined from Yourshaw *et al.* (Ref. 46).

eKE of feature B_1 to the measured values in the above study, using linear interpolation to obtain a fractional $\langle n_{I^-} \rangle$ when the energy lies between measured shifts. Figure 5 shows the eKE of feature B_1 vs time for all clusters, with $\langle n_{I^-} \rangle$, indicated on the right-hand side of the figure. For $I_2^-(Ar)_{n \geq 12}$, the graph stops when the feature begins to decrease in energy and is relabeled D_1; this change in direction is associated with recombination on the I_2^- $\tilde{A}$ state,[12,28] so that the peak no longer reflects a pure I^- signal.

To determine the contribution of solvated I^- to the FPE spectra, $I^-(Ar)_n$ features were simulated from a measured probe-only spectrum of bare I^- and shifted in energy according to the known solvent shift. The integrated intensity of the $I\,^2P_{3/2} \leftarrow I^-\,^1S_0$ transition was taken to be 2.0 (see Table III), relative to 1.0 for the I_2 $\tilde{X} \leftarrow I_2^-$ $\tilde{X}$ ($v=0$) transition as determined by comparing the integrated intensities of I_2^- bleach and I^- (signal) features in the FPES of bare I_2^-. The intensity of the $I\,^2P_{1/2} \leftarrow I\,^1S_0$ transition was empirically determined to be 0.6. The final spectrum was convoluted with an instrument resolution function,[33] calibrated approximately for experimental conditions.

B. Bare and solvated $I_2^-(\tilde{X})$

We next consider the contribution to the spectra from bare and solvated I_2^- in various vibrational levels resulting from recombination on the $\tilde{X}$ state. The I_2^- $\tilde{X}$ state potential parameters and I_2 neutral state parameters were taken from Zanni *et al.*,[34,44] with the exception of the I_2 $\tilde{B}'$ state, for which the repulsive wall was adjusted empirically to fit a high-resolution (~10 meV) photoelectron spectrum of I_2^-.[38] Anion wave functions were calculated using standard procedures for a Morse oscillator,[47] and a photoelectron spectrum for each vibrational level was generated using a time-dependent propagation method[48] to calculate the Franck–Condon overlap with various neutral states. It was assumed that spectra arose from an incoherent superposition of vibrational levels, so composite spectra were constructed by summing spectra from individual vibrational wavefunctions over a distribution of levels.

TABLE II. Parameters used in the $f(E)$ function for scaling the $I_2\tilde{X} \leftarrow I_2^-\tilde{X}$ transition. See Eq. (1) in text.

Parameter	Value
a_1	0.4–1.0[a]
a_2	1.6
k_1	−0.02 eV
k_2	0.08 eV
E_1	1.3 eV
E_2	2.0 eV

[a]Varied with $\langle v \rangle$.

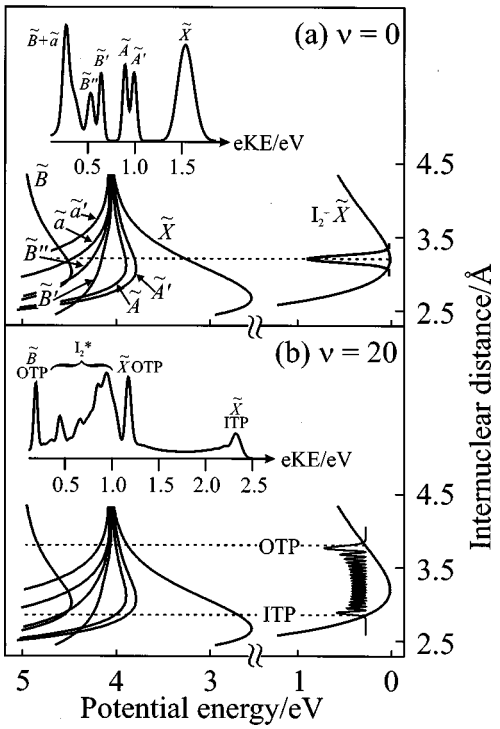

FIG. 6. Simulated photoelectron spectra from (a) $v=0$ and (b) $v=20$ levels of $I_2^-(\tilde{X})$.

The effect of anion vibrational excitation can be seen in Fig. 6, which shows two simulated photoelectron spectra of the I_2^- $\tilde{X}$ state and their relation to the I_2 potential energy curves for (a) $v=0$ and (b) $v=20$. The vibrationally cold spectrum ($v=0$) consists of an extended progression, unresolved at the resolution of the FPE spectrometer, centered at 1.54 eV (the I_2 $\tilde{X}$ state), a pair of narrow features at 1.00 eV [$\tilde{A}'(^3\Pi_{2u})$] and 0.90 eV [$\tilde{A}(^3\Pi_{1u})$], another pair of narrow features at 0.65 eV [$\tilde{B}'(^3\Pi_{0^-u})$] and 0.54 eV [$\tilde{B}''(^1\Pi_u)$], and two broad, overlapping features at ~0.30 eV [$\tilde{a}(^3\Pi_{1g})$ and $\tilde{B}(^3\Pi_{0^+u})$]. The $\tilde{a}'(^3\Sigma^-_{0^+g})$ state is not seen, since it is not accessible at the probe photon energy from I_2^- $\tilde{X}$ ($v=0$).

For the vibrationally excited $\tilde{X}$ state ($v=20$), the shapes and energies of the photoelectron features change considerably. Since the amplitude of the $\tilde{X}$ state wave function is concentrated near the classical inner and outer turning points of the potential (ITP and OTP, respectively), Franck–Condon overlap with I_2 states will be largest in these regions. For the I_2 $\tilde{X} \leftarrow I_2^-$ $\tilde{X}$ transition, the large change in I_2 $\tilde{X}$ po-

tential energy with internuclear distance produces distinctive and well-separated features arising from each region; an extended tail at high eKE, arising from the ITP region, and a narrower, intense peak at low eKE due to the OTP region. The ITP region of the spectrum is very sensitive to v, whereas the OTP region is fairly independent of v over the range $v \sim 10-30$ because the anion and neutral potential energy curves are approximately parallel. At higher vibrational levels, the OTP energy increases with v. For the $\tilde{A}' \leftarrow \tilde{X}$ and $\tilde{A} \leftarrow \tilde{X}$ transitions, the difference in eKE between the ITP and OTP regions is much less, though there is a considerable broadening for $v > \sim 30$. The $\tilde{B}'$, $\tilde{B}''$, $\tilde{a}$, and $\tilde{a}'$ states display a wider range of potential energies, so that the OTP regions of these transitions overlap with the $\tilde{A}'/\tilde{A} \leftarrow \tilde{X}$ transition, and the ITP regions occur at much lower eKE. The $\tilde{B} \leftarrow \tilde{X}$ transition, correlating at large internuclear distance with the $I\,^2P_{1/2} \leftarrow I^-\,^1S_0$ transition, appears near 200 meV for $v \leqslant 60$.

Solvation by Ar atoms shifts the I_2^- features toward lower eKE by stabilizing the anion more than the neutral, much as for $I^-(Ar)_n$. These solvent shifts have been measured for vibrationally cold $I_2^-(Ar)_n$ clusters using photoelectron spectroscopy,[38] and are used to shift the simulated spectra. The shifts are smaller than for $I^-(Ar)_n$, despite the fact that the $I_2^- - Ar$ binding energy (53 meV) is larger than that of $I^- - Ar$ (45.8 meV);[46] this is due to a somewhat larger $I_2 - Ar$ binding energy over that of I–Ar. It is assumed that the shifts do not change for $v > 0$. Note that the $I_2^- - Ar$ bond energy is significantly lower than the average energy lost by the cluster when an Ar atom evaporates; this was found by Vorsa *et al.*[7] to be 73 meV from the number of solvent atoms remaining in I_2^- fragments from large ($n > 20$) parent clusters. This discrepancy is attributed to kinetic energy of the departing Ar atom.[7]

The simulated spectra in Fig. 6 support the assignment of the experimental features E and F in Table I. From the shape and energy of these features it should be possible to determine $\langle v \rangle$, the average I_2^- vibrational quantum number, and $\langle n_x \rangle$, the average number of solvent atoms. In practice, we find that when $\langle v \rangle$ is very small ($< \sim 5$), the $\tilde{X} \leftarrow \tilde{X}$ transition is compact and the shape depends sensitively on $\langle v \rangle$, so both $\langle n_x \rangle$ and $\langle v \rangle$ may be simultaneously determined by simulating the shape and energy of feature E. For larger $\langle v \rangle$, the $\tilde{X} \leftarrow \tilde{X}$ ITP energy is mostly governed by $\langle v \rangle$, but $\langle n_x \rangle$ strongly modifies it, so feature E cannot be used to determine $\langle v \rangle$ exclusively. However, feature F, arising from the $\tilde{X} \leftarrow \tilde{X}$ OTP and $\tilde{A}'/\tilde{A}/\tilde{B}'/\tilde{B}''/\tilde{a}/\tilde{a}'/\tilde{B}$ (collectively referred to as I_2^*) $\leftarrow \tilde{X}$ transitions, is more sensitive to $\langle n_x \rangle$ than to $\langle v \rangle$. For $\langle v \rangle$ between 5 and 30, two distinct peaks are visible which can be used in conjunction with the $\tilde{X} \leftarrow \tilde{X}$ ITP transition to obtain both $\langle v \rangle$ and $\langle n_x \rangle$. For $\langle v \rangle$ larger than 30, the $\tilde{X} \leftarrow \tilde{X}$ OTP and $I_2^* \leftarrow \tilde{X}$ transitions coalesce into a single, broad peak, and determination of $\langle n_x \rangle$ is less precise.

Finally, we discuss how the intensities in the contributions to the simulated spectra from $I_2^-(\tilde{X})$ are obtained. There are two issues here: the failure of the Franck–Condon approximation for photodetachment from high vibrational levels of I_2^-, and the presence of photodetachment transitions to multiple neutral electronic states. Our analysis shows that the portions of the FPE spectra corresponding to $\tilde{X} \leftarrow \tilde{X}(v \gg 0)$ transitions cannot be fit unless the photodetachment transition dipole varies with eKE as well as v. For example, at large v (>30), one needs to scale the intensity in the ITP and OTP regions by 1.6 and 0.4, respectively, to fit the experimental spectra. This breakdown of the Franck–Condon approximation is not unexpected, since the wavefunctions are quite extended for vibrationally excited levels, and the overlap of the electronic orbitals will be significantly different than at the equilibrium bond distance, changing the relative cross section. Therefore, to obtain the best estimate of the true integrated intensities, an energy-dependent scaling function $f(E)$ was applied to the simulated spectra for the $\tilde{X} \leftarrow \tilde{X}$ transition,

$$f(E) = \frac{a_1 - 1}{1 + e^{-(E-E_1)/k_1}} + \frac{a_2 - 1}{1 + e^{-(E-E_2)/k_2}} + 1, \qquad (1)$$

where E is electron kinetic energy (eV) before applying any solvent shifts. Parameters for this function are summarized in Table II. Note that a_1, which governs the $\tilde{X} \leftarrow \tilde{X}$ OTP intensity, was varied in different spectra from 0.4 to 1.0, following an inverse trend with $\langle v \rangle$, which indicated a decreasing transition dipole moment as the internuclear radius increased.

The integrated intensities of transitions from the I_2^- $\tilde{X}$ state to the other I_2 electronic states were empirically determined using the one-photon spectrum of bare $I_2^-(v=0)$ and normalizing the $\tilde{X} \leftarrow \tilde{X}$ transition to 1.0 as a reference. The work of Asmis *et al.*[38] showed that these intensities do not change in $I_2^-(Ar)_n$ clusters. However, further scaling of the $\tilde{a}/\tilde{a}' \leftarrow \tilde{X}$ and $\tilde{B} \leftarrow \tilde{X}$ transitions improved our fits for some of the spectra; this might result again from problems associated with the Franck–Condon approximation. In any case, the overall effect of these additional scaling factors is more cos-

TABLE III. Relative integrated intensities of transitions used in simulated spectra.

Transition	Relative integrated intensity
$I_2\tilde{X} \leftarrow I_2^-\tilde{X}\,(v=0)$	1.0
$I_2\tilde{X} \leftarrow I_2^-\tilde{X}\,(v>0)$	0.4–1.6[a]
$I_2\tilde{A}'/\tilde{A} \leftarrow I_2^-\tilde{X}$	0.24
$I_2\tilde{B}'\tilde{B}'' \leftarrow I_2^-\tilde{X}$	0.2
$I_2\tilde{a} \leftarrow I_2^-\tilde{X}$	0.15–0.5[b]
$I_2\tilde{a}' \leftarrow I_2^-\tilde{X}$	$1.5\times(I_2\tilde{a} \leftarrow I_2^-\tilde{X})$
$I_2\tilde{B} \leftarrow I_2^-\tilde{X}$	0.5–1.0[b]
$I_2\tilde{A}'/\tilde{A}/\tilde{B}'/\tilde{B}'' \leftarrow I_2^-\tilde{A}$	0.22
$I_2\tilde{a} \leftarrow I_2^-\tilde{A}$	0.44
$I_2\tilde{a}' \leftarrow I_2^-\tilde{A}$	0.66
$I_2\tilde{B} \leftarrow I_2^-\tilde{A}$	0.6
$I\,^2P_{3/2} \leftarrow I^-\,^1S_0$	2.0
$I\,^2P_{1/2} \leftarrow I\,^1S_0$	0.6

[a]Spectra scaled with energy-dependent function $f(E)$; see below and text.
[b]Varied with spectrum.

TABLE IV. Number of solvent atoms $\langle n_{I^-} \rangle$ for feature B_1 at ~300 fs, along with estimated $\langle n_{I^-} \rangle$ for anomalous and normal charge-switching states, calculated from model structures.[a]

Parent cluster	B_1	Anomalous	Normal
6	4.7	6.0	6.0
9	5.4	6.0	9.0
12	5.8	6.0	12.0
16	9.1	9.0	13.0
20	13.3	13.0	13.0

[a]References 28 and 39.

metic than essential; they improve the fit but have little influence on the important conclusions drawn from the FPE spectra. The scaling factors used are given in Table III.

C. Bare and solvated $I_2^-(\tilde{A})$

As mentioned in the Results, peaks D_1 and D_2 in the $n \geqslant 12$ spectra are primarily due to photodetachment from the I_2^- $\tilde{A}$ state. Simulation of these features is less precise than for those arising from the $\tilde{X}$ state, in part because no spectroscopic data are available for the $\tilde{A}$ state. A Morse function was assumed, using parameters $R_e = 4.7$ Å and $D_e = 140$ meV. These are slightly modified from Greenblatt *et al.*[12] to better fit the $I_2^-(Ar)_{20}$ spectrum at 3 ns, assuming that evaporation is complete by this time so that the number of solvent atoms ($\langle n_A \rangle$) was equal to the average value of 11.1 found in the photofragmentation experiments.[6] This assumption is supported by the simulations of Faeder *et al.*[28] but may be problematic (see Discussion).

Transitions from the $v = 0$ level of the $\tilde{A}$ state to each neutral state were weighted equally (except to the $\tilde{X}$ state, which is not accessible by a one-electron transition[33]), as was done by Zanni *et al.* for the I_2^- $\tilde{A}'$ state.[44] In many of the spectra, peak D_1 is broader than peak D_2. The larger width of D_1 is likely due to the repulsive regions of the I_2 states ($\tilde{B}'$, $\tilde{B}''$, $\tilde{a}$, $\tilde{a}'$), but as these are poorly defined, adequate reproduction of this broadening was not possible. The simulation of this feature was therefore convoluted with a resolution function of width ~250 meV.

The number of solvating Ar atoms, $\langle n_A \rangle$, was determined from the experimental spectra using the energy shifts of the $I^-(Ar)_n$ clusters, rather than the $I_2^-(Ar)_n$ clusters. This choice is based on the expectation that at the large internuclear distances characteristic of the $\tilde{A}$ state, solvation effects will localize the excess electron on a single I atom to a much larger extent than for the $\tilde{X}$ state, so that I^- rather than I_2^- solvent shifts are more appropriate. This assumption was borne out in other clusters by fairly good agreement between the calculated values for $\langle n_A \rangle$ at long time delays and the photofragmentation averages (see Discussion). The integrated intensity was assumed to be the same as for I^-, which was also supported experimentally.

D. State populations and simulations of the spectra

For the $n \leqslant 9$ clusters, no recombination occurs, and $\langle n_{I^-} \rangle$ can be obtained by inspection of the peak positions.

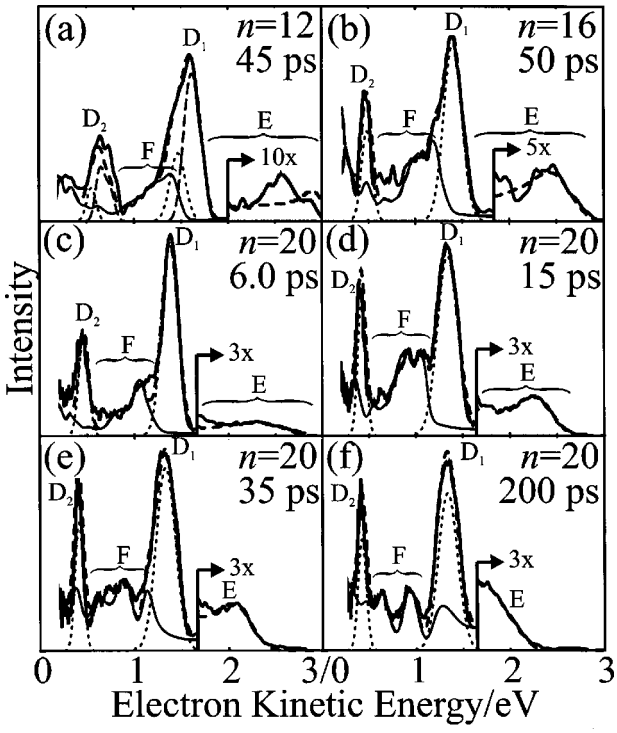

FIG. 7. Experimental (thick solid) and simulated (thick dashed) FPE spectra of $I_2^-(Ar)_n$ clusters at selected time delays. (a) $I_2^-(Ar)_{12}$,45 ps; (b) $I_2^-(Ar)_{16}$,50 ps; (c) $I_2^-(Ar)_{20}$,6.0 ps; (d) $I_2^-(Ar)_{20}$,15 ps; (e) $I_2^-(Ar)_{20}$,50 ps; (f) $I_2^-(Ar)_{20}$,200 ps. Contributions to simulations are shown from $\tilde{X}$ state (thin solid line), $\tilde{A}$ state (dotted line), and solvated I^- (thin dashed line). Features in spectra are labeled as in Table I.

Numerous time delays have been simulated to follow the dynamics in clusters of $I_2^-(Ar)_{n \geqslant 12}$, and selected examples are shown in Fig. 8. For $I_2^-(Ar)_{12,16}$, where changes are minimal once features *E* and *F* have appeared, only a single, long time delay (45–50 ps) is shown in Figs. 7(a)–7(b). In $I_2^-(Ar)_{20}$, where significant evolution is observed in the spectra after the appearance of these features, several time delays (6.0, 15, 35, and 200 ps) are shown in Figs. 7(c)–7(b). Each figure includes curves representing the I^- [for $I_2^-(Ar)_{12}$ only], $I_2^-\tilde{X}$ and $I_2^-\tilde{A}$ contributions, the total simulated spectrum, and the experimental spectrum. Simulation parameters are summarized in Table V. Populations of the I^-, $I_2^-(\tilde{X})$, and $I_2^-(\tilde{A})$ contributions, indicated by P_{I^-}, P_X, and P_A, respectively, were determined from the intensities of simulated spectral features, weighted by their relative cross sections. Populations sum to unity for all spectra and are listed in Table V.

In Fig. 8, P_X is plotted vs time for all three clusters, for many more time delays than shown in Fig. 7. Photofragmentation values are indicated as detached points on the right-hand side of the graph. As $I_2^-(Ar)_{20}$ displays considerable vibrational relaxation not seen in the smaller clusters, Figs. 9(a)–9(b) plots $\langle v \rangle$ and $\langle n_X \rangle$ vs time for this cluster, along with model data from Faeder *et al.*[28] Figure 9(c) plots a derived quantity E_{cluster} which is defined in the section on $I_2^-(Ar)_{20}$ in the Discussion.

TABLE V. Parameters used in simulating spectra of $I_2^-(Ar)_n$ clusters at selected time delays. P_X, P_A, and P_{I^-} indicate populations of $I_2^-\,\tilde{X}$, $I_2^-\,\tilde{A}$, and I^- fragments, respectively. $\langle v\rangle$ indicates the average vibrational level of the $I_2^-\,\tilde{X}$ state. $\langle n_X\rangle$, $\langle n_A\rangle$, and $\langle n_{I^-}\rangle$ indicate the average numbers of Ar atoms surrounding the $I_2^-\,\tilde{X}$, $I_2^-\,\tilde{A}$, and I^- fragments, respectively. ''MS'' indicates results of photofragment experiments from Vorsa *et al.* (Refs. 6 and 7).

Parent cluster	Time (ps)	Population			$I_2^-\,\tilde{X}$	Number of Ar		
		P_X	P_A	P_{I^-}	$\langle v\rangle$	$\langle n_X\rangle$	$\langle n_A\rangle$	$\langle n_{I^-}\rangle$
12	45	0.30	0.21	0.49	68.0	0	5.0	3.2
	MS	0.23	0.23	0.54	···	0	2.3	3.2
16	50	0.50	0.50	0	34.4	0	8.0	···
	MS	0.43	0.55	0.02	···	0	6.2	8.5
20	6.0	0.36	0.64	0	40.0	8.0	9.0	···
	15	0.50	0.50	0	29.1	6.0	11.0	···
	35	0.50	0.50	0	14.2	3.0	11.5	···
	200	0.54	0.46	0	5.6	0.5	11.0	···
	MS	0.44	0.56	0	···	0.2	11.1	···

V. DISCUSSION

This section of the paper is divided into four parts. In the first section, the FPE spectra around 300 fs are examined for all clusters, in order to determine the initial configuration of solvent atoms around the newly formed I^- fragment. In the second section, $I_2^-(Ar)_6$ and $I_2^-(Ar)_9$ clusters are discussed; no recombination occurs in either case. This is followed by a discussion of $I_2^-(Ar)_{12}$ and $I_2^-(Ar)_{16}$ FPE spectra, which display $I_2^-\,\tilde{A}$ state and $I_2^-\,\tilde{X}$ state features, but limited vibrational relaxation in the $\tilde{X}$ state. Finally, $I_2^-(Ar)_{20}$ is examined separately, since its spectra display extensive $\tilde{X}$ state vibrational relaxation in addition to the dynamics observed in smaller clusters.

A. Initial solvent configuration in the $\tilde{A}'$ state

In all clusters studied here, a peak associated with solvated I^- is first observed ~ 300 fs after the pump pulse. Simulations of the cluster dynamics indicate that the even though the interiodine separation has increased to ~ 6Å during this interval, the Ar atoms move very little.[28] Hence, the number of Ar atoms $\langle n_{I^-}\rangle$ interacting with the I^- at 300 fs reflects the initial configuration of the Ar atoms in the clus-

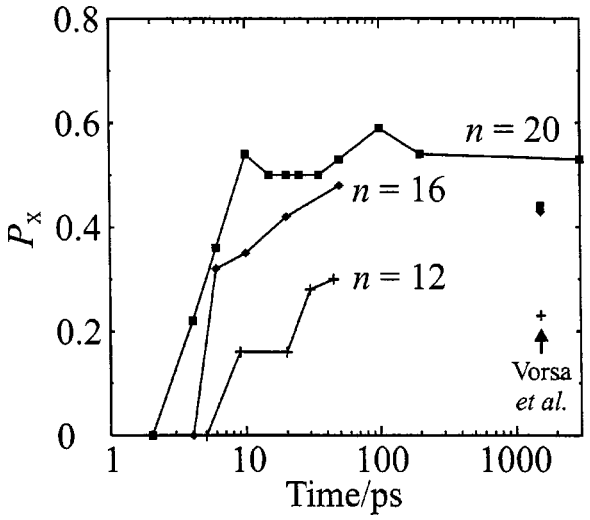

FIG. 8. Population of the $I_2^-\,\tilde{X}$ state (P_X) vs time, for $I_2^-(Ar)_{n\geq 12}$ clusters: $I_2^-(Ar)_{12}$ (crosses), $I_2^-(Ar)_{16}$ (diamonds), $I_2^-(Ar)_{20}$ (squares). Detached points indicate photofragmentation averages from Vorsa *et al.* (Ref. 6).

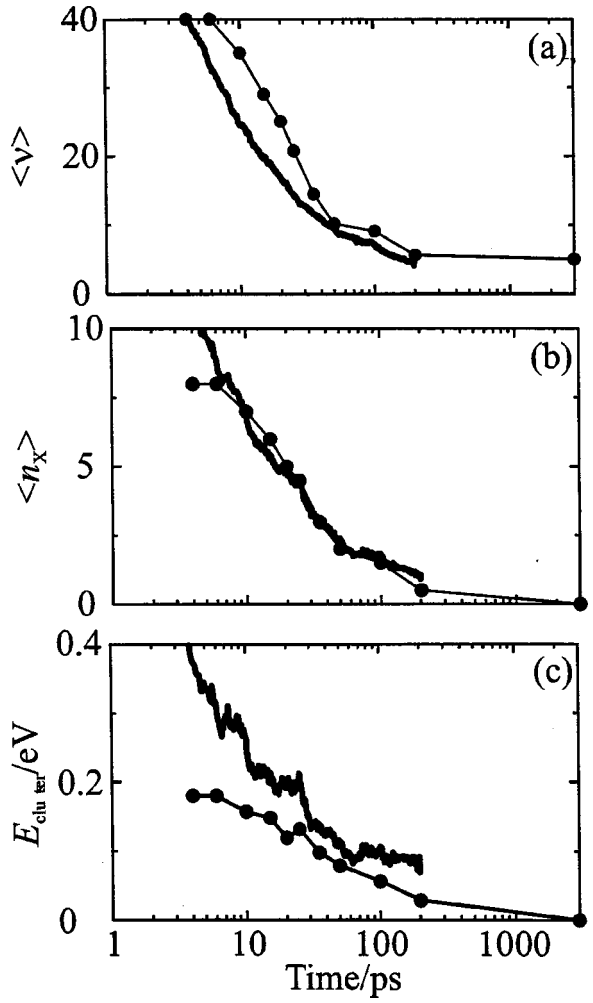

FIG. 9. (a) Average $I_2^-\,\tilde{X}$ state vibrational level ($\langle v\rangle$), (b) average number of the $I_2^-\,\tilde{X}$ state solvent atoms ($\langle n_X\rangle$), and (c) excess cluster energy ($E_{cluster}$) vs time for $I_2^-(Ar)_{20}$ from the FPE spectra (circles and thin line) and from Faeder *et al.* (Ref. 28) (thick line).

ter. Table IV shows a comparison of $\langle n_{I^-} \rangle$ at 300 fs, when dissociation has just occurred, with estimates of $\langle n_{I^-} \rangle$ for the solvent configurations in anomalous and normal charge-switching states, as defined in the Introduction. These estimates represent the number of Ar atoms coordinated to the I atom with less (anomalous) and more (normal) negative charge according to the calculated ground state structures.[24,25,39] If, just after excitation, the electron is localized on the original, more solvated I atom (the case on the $\tilde{X}$ and $\tilde{A}$ states) at 300 fs, then the experimentally-determined $\langle n_{I^-} \rangle$ will be close to the estimated number for a normal charge-switching state. On the other hand, if the electron has jumped to the less-solvated I atom (as predicted for the $\tilde{A}'$ state),[21] then the $\langle n_{I^-} \rangle$ will lie close to the anomalous charge-switching state estimate.

We note that (a) the two estimates are equal for $I_2^-(Ar)_6$ and $I_2^-(Ar)_{20}$, since the solvent configuration of these clusters is calculated to be symmetric, and the experimental values for $\langle n_{I^-} \rangle$ are in good agreement in both cases, (b) for $I_2^-(Ar)_{9,12,16}$, in which the calculated solvent configuration is very asymmetric, the estimate for the anomalous charge-switching state is considerably lower (by 3–6 atoms) than for the normal state, and (c) for those three clusters, the experimental value of $\langle n_{I^-} \rangle$ is clearly closer to the estimate for the anomalous charge-switching state. This comparison provides direct experimental support for the prediction that the excess electron is localized on the less solvated I atom immediately after photoexcitation to the $\tilde{A}'$ state, thus identifying the $\tilde{A}'$ state as an anomalous charge-switching state.

B. $I_2^-(Ar)_6$ and $I_2^-(Ar)_9$

For these two clusters, the increase in the eKE of the *B* features after $\sim$ 300 fs results from a decreasing number of solvent atoms surrounding I^-; Fig. 5 shows that $\langle n_{I^-} \rangle$ decreases until $\sim$ 1.5 ps. One possible explanation for the decrease is that the loss of solvent is due to fast ejection of neutral I, leaving behind a vibrationally excited $I^-(Ar)_n$ cluster which evaporates Ar atoms until the available energy is dissipated. This mechanism was suggested in studies of $Br_2^-(CO_2)_n$ clusters.[19] However, theoretical simulations by Faeder *et al.*[25,28] predict that, in small clusters such as $I_2^-(Ar)_6$, the I^- fragment simply leaves the cluster, capturing one or more Ar atoms during its escape. Hence, as discussed previously,[12] the decrease in $\langle n_{I^-} \rangle$ reflects the steady weakening of the attractive interaction between the I^- and Ar solvent atoms.

For $I_2^-(Ar)_6$, little change occurs after 1.5 ps, at which point the value of $\langle n_{I^-} \rangle$ (1.2), just slightly higher than the photofragmentation average[7] of 0.9 (indicated in Fig. 5). Figure 5 shows that $\langle n_{I^-} \rangle$ does decrease to this value by 50 ps, presumably due to Ar atom evaporation from $I^-(Ar)_{m>1}$ fragments.

In $I_2^-(Ar)_9$, however, there is an increase in $\langle n_{I^-} \rangle$ of 1.5 between 2.8 and 12 ps, followed by a decrease of 0.5 through 100 ps. The increase in $\langle n_{I^-} \rangle$ does not, occur for $I_2^-(Ar)_6$, but a similar effect was seen in the FPES of $I_2^-(CO_2)_4$.[13] We attribute this effect to ''arrested dissociation'' on the $\tilde{A}'$ state; the less-solvated I^- atom initially moves away from the cluster due to the repulsive $\tilde{A}'$ state potential, but cannot leave the cluster because of the attractive interaction with the Ar atoms surrounding the more solvated neutral I atom. Instead the solvent atoms rearrange to a more symmetric configuration, and a transition to the $\tilde{X}$ or $\tilde{A}$ state occurs. This results in more solvation of the I^- at the expense of the neutral I atom which can then easily leave the cluster.

This interpretation is consistent with dynamics calculations by Faeder *et al.*[25] They observed transitions to the $\tilde{A}$ state without recombination and found these transitions to be responsible for the high-mass $I^-(Ar)_n$ channel observed by Vorsa *et al.* in clusters of $I_2^-(Ar)_{n\geq 11}$,[6,7] since the solvent can more effectively surround the I^- in a normal charge-switching state. Although not reported in the paper, their model also observes transitions prior to final dissociation in clusters of $I_2^-(Ar)_9$.[49] In $I_2^-(CO_2)_n$ clusters, this electronic transition mechanism is present in all cluster sizes and occurs as rapidly as $\sim$ 500 fs in large clusters.[35]

For $I_2^-(Ar)_9$, the long-time (>12 ps) decrease in $\langle n_{I^-} \rangle$ is probably due to solvent evaporation. $\langle n_{I^-} \rangle$ exceeds the photofragmentation average (2.7) by 1.0 after the electronic transition to the $\tilde{X}/\tilde{A}$ state, and the value at 100 ps is still larger than the photofragmentation average by 0.5 Ar atoms. The small discrepancy between the photofragmentation average and the FPES value of $\langle n_{I^-} \rangle$ at 100 ps suggests that further evaporation occurs after 100 ps.

C. $I_2^-(Ar)_{12}$ and $I_2^-(Ar)_{16}$

In these two clusters, the increase in the eKE of the *B* features is similar to that of the smaller clusters, and also occurs over a $\sim$1–2 ps time scale, as seen in Fig. 5. In the case of $I_2^-(Ar)_{12}$, the associated decrease in $\langle n_{I^-} \rangle$ is due to a combination of I^- pulling away from the cluster and large amplitude motion of the I atoms within the cluster at short delay times, possibly coupled with solvent evaporation. However, the cage fraction from $I_2^-(Ar)_{16}$ is essentially unity, so only the second process can occur.

According to the photofragmentation study,[7] there is substantial recombination of I_2^-, with virtually no I^- remaining in $I_2^-(Ar)_{16}$. In the FPE spectra, features *E* and *F* appear by $\sim$10 ps in each cluster, indicating recombination of I_2^- on the $\tilde{X}$ state. The broadening of the *D* features after 2.0–2.5 ps, and the shifting toward lower eKE, which is particularly pronounced (240 meV) for $I_2^-(Ar)_{16}$, indicate recombination on the $\tilde{A}$ state. Because these spectra no longer indicated the presence of exclusively I^-, simulations were required in order to characterize the dynamics after these time delays.

In $I_2^-(Ar)_{12}$, although the *D* features broaden through the longest time delay measured, and the intensities of features *E* and *F* also grow slowly throughout this time range, there is little change in shape to any of these features after their formation by $\sim$ 10 ps. Only the spectrum at 45 ps is shown in Fig. 7(a), since this is the FPE spectrum in which feature *E* is most intense. Unfortunately, event at 45 ps, the poor signal to noise ratio in the region of this feature made accurate determination of $\langle v \rangle$ difficult. We therefore set $\langle v \rangle = 68$ and $\langle n_X \rangle = 0$, the value consistent with the calculated available energy after evaporation of all 12 Ar atoms (710

meV) assuming 73 meV per Ar atom. Complete loss of solvent is consistent with Vorsa *et al.*,[6,7] who observed $\langle n_X \rangle = 0$ in their photofragmentation study.

Using $\langle v \rangle = 68$ as a starting point, an $\tilde{X}$ state vibrational distribution was constructed with $P_X = 0.30$ and $\langle n_X \rangle = 0$. Although the $\tilde{X} \leftarrow \tilde{X}$ITP transition does not accurately reproduce feature *E*, error bars in the intensity are estimated at 20%–30%, and the overall intensity in this region is comparable to the simulation. The $\tilde{X} \leftarrow \tilde{X}$OTP and $I_2^* \leftarrow \tilde{X}$ transitions together account for much of the broad feature *F*. P_X is close to the photofragmentation value (0.23). D_1 was represented by a combination of solvated $I_2^-(\tilde{A})$ and I^-, using the following parameters: $P_A = 0.21$, $P_{I^-} = 0.49$, $\langle n_A \rangle = 5.0$, and $\langle n_{I^-} \rangle = 3.2$. The eKE of D_2 is also accounted for by the excited spin–orbit transitions from these states, though the intensity is lower than in the observed spectrum. The populations of the $I_2^-(\tilde{A})$ and I^- channels are close to the photofragmentation values (0.23 and 0.54, respectively; see Table V), and $\langle n_{I^-} \rangle$ is equal to the measured average. $\langle n_A \rangle$, however, is larger than the photofragmentation average of 2.3; the larger value was necessary in order to adequately simulate the spectrum.

P_X is plotted vs time in Fig. 8 for several time delays between 3.5 and 45 ps. Population appears by 9.0 ps, and grows in slowly through 45 ps. The slow, monotonic increase in the width of the *D* features over this time interval (see Fig. 4) indicates a similarly slow growth of the $I_2^- \tilde{A}$ state, and the large value of $\langle n_A \rangle$ at 45 ps compared to the photofragmentation average also indicates incomplete dynamics on this state. Both $\langle n_X \rangle$ and $\langle n_{I^-} \rangle$, however, are equal to the photofragmentation averages. Thus, only the $\tilde{A}$ state has not finished evaporation by 45 ps. This is consistent with the MD simulations of Batista[24] and Faeder *et al.*[25,28] which showed that only $\tilde{A}$ state evaporation required longer than the 50 ps length of the simulation for completion.

In the FPES of $I_2^-(Ar)_{16}$, the shifts in the *D* features are complete by 20 ps. After features *E* and *F* have appeared at 10 ps, they evolve slightly through 50 ps, but $\langle v \rangle$ for the $\tilde{X}$ state decreases only by ~5 during this interval. Therefore, only the 50 ps spectrum is shown in Fig. 7(b), with the following parameters: $P_X = 0.50$, $P_A = 0.50$, $\langle v \rangle = 34.4$, $\langle n_X \rangle = 0$ and $\langle n_A \rangle = 8.0$. P_X and P_A are close to the photofragmentation results (0.43 and 0.57, respectively). $\langle v \rangle$ corresponds almost exactly to the calculated energy remaining in the cluster after evaporation of all 16 Ar atoms (420 meV). This result supports the assumption that $\langle n_X \rangle = 0$, which is also the long-time limit set by the photofragmentation study. Feature *E* is reproduced by the $\tilde{X} \leftarrow \tilde{X}$ITP transition, while *F* is accounted for by the overlapping $\tilde{X} \leftarrow \tilde{X}$ OTP and $I_2^* \leftarrow \tilde{X}$ transitions. Features D_1 and D_2 were simulated by the $\tilde{A}$ state. The value of $\langle n_A \rangle (8.0)$ is actually larger than $\langle n_{I^-} \rangle$ at 2.0 ps (5.0), reflecting the expected solvent rearrangement on the normal charge-switching state, much as was seen in $I_2^-(Ar)_9$. However, as $\langle n_A \rangle$ is larger than the photofragment average (6.2), further evaporation must occur on a longer time scale, as also inferred for $I_2^-(Ar)_{12}$.

P_X is plotted vs time in Fig. 8 for several simulated time delays. It rises faster, and is larger at all time delays than that of $I_2^-(Ar)_{12}$, though it never achieves a plateau value. However, since P_X at 50 ps is roughly the same as the photofragmentation value, population transfer to the $\tilde{X}$ state (i.e., recombination) appears to be complete. The same holds for vibrational relaxation, since $\langle v \rangle$ agrees with the long-term value at 50 ps.

D. $I_2^-(Ar)_{20}$

In the $I_2^-(Ar)_{20}$ FPE spectra, the decrease in $\langle n_{I^-} \rangle$ of feature *B* through 1.0 ps is slightly less than in the smaller clusters (2.6 vs ~3–4). As with $I_2^-(Ar)_{16}$, this decrease must be due to a combination of large amplitude motion and solvent evaporation. At later times, recombination on the $I_2^- \tilde{A}$ state is responsible for the shifting toward lower eKE (140 meV by 200 ps) and the broadening apparent after 6 ps. The evolution of features *E* and *F* indicate extensive vibrational relaxation on the $I_2^- \tilde{X}$ state. Several time delays were simulated (6.0 ps, 15 ps, 50 ps, 200 ps) to follow this process, shown in Figs. 7(c)–7(f). P_X for these and other delays are shown in Fig. 8.

In the 6.0 ps spectrum ($P_X = 0.36$, $P_A = 0.64$, $\langle v \rangle = 44.5$, $\langle n_X \rangle = 8.0$, $\langle n_A \rangle = 9.0$), the $I_2^- \tilde{X}$ state is still in the process of growing in. It is also so vibrationally excited that the relative intensity of the $\tilde{X} \leftarrow \tilde{X}$ OTP transition appears to be changing rapidly in this range; thus, feature *F* above 1.0 eV is difficult to simulate accurately. At lower eKE, however, the $I_2^* \leftarrow \tilde{X}$ transitions accounts for much of the intensity of feature *F*, while the $\tilde{X} \leftarrow \tilde{X}$ ITP transition reproduces feature *E* satisfactorily. $\langle n_X \rangle$ is also difficult to determine from feature *F*, but an approximate upper limit is obtained by matching the falling edge near 1.0 eV. The $\tilde{A}$ state, accounting for D_1 and D_2, has a smaller apparent number of Ar atoms than at later time delays, and D_1 is also not as broad. This probably reflects a wavepacket that is still in the process of moving into the $\tilde{a}$ state well, giving an artificially low value of $\langle n_A \rangle$.

The spectra at 15 ps ($P_X = 0.50$, $P_A = 0.50$, $\langle v \rangle = 29.0$, $\langle n_X \rangle = 6.0$, $\langle n_A \rangle = 11.0$) and 35 ps ($P_X = 0.50$, $P_A = 0.50$, $\langle v \rangle = 14.2$, $\langle n_X \rangle = 3.0$, $\langle n_A \rangle = 11.5$) show the effects of progressive vibrational relaxation and solvent evaporation for the $\tilde{A}$ state. The $\tilde{X} \leftarrow \tilde{X}$ ITP transition comprising feature *E* shifts toward lower energy. At 15 ps, feature *F* displays two peaks which are reproduced in the simulation, corresponding to the $\tilde{X} \leftarrow \tilde{X}$ OTP transition at higher eKE, and the $I_2^* \leftarrow \tilde{X}$ transitions at lower eKE. At 35 ps, the $\tilde{A}'/\tilde{A} \leftarrow \tilde{X}$ and $\tilde{B}'/\tilde{B}'' \leftarrow \tilde{X}$ transitions appear as separate peaks at 900 and 610 meV, respectively, while the $\tilde{X} \leftarrow \tilde{X}$ OTP transition appears as a small shoulder on the low eKE side of feature D_1. This splitting of feature *F* enabled accurate determination of $\langle n_X \rangle$ at both delays. The $\tilde{A}$ state contribution to the spectra undergoes no significant evolution after 15 ps.

The 200 ps spectrum ($P_X = 0.54$, $P_A = 0.46$, $\langle v \rangle = 5.6$, $\langle n_X \rangle = 0.5$, $\langle n_A \rangle = 11.0$) shows that the $I_2^- \tilde{X}$ state is almost

completely relaxed. While the $\tilde{X} \leftarrow \tilde{X}$ ITP transition accounts for feature *E*, the OTP transition falls completely under D_1. Feature *F* consists of the $\tilde{A}'/\tilde{A} \leftarrow \tilde{X}$ and $\tilde{B}'/\tilde{B}'' \leftarrow \tilde{X}$ transitions, which are clearly separated with considerably less intensity between the peaks than at 35 ps, allowing accurate determination of $\langle n_X \rangle$. The $\tilde{A}$ state again accounts for D_1 and D_2.

P_X in Fig. 8 rises more rapidly than in the smaller clusters, achieving a plateau near ~0.55 by 10 ps, before either vibrational relaxation or solvent evaporation has neared completion. This distinction between recombination and relaxation was not visible in $I_2^-(Ar)_{12}$ or $I_2^-(Ar)_{16}$, where relaxation has proceeded almost as far as possible by the time significant $\tilde{X}$ population was present.

$\tilde{A}$ state relaxation and evaporation appears complete by ~15 ps, soon after P_X reaches its final value at 10 ps, as indicated by the plateauing of $\langle n_A \rangle$ in the simulations. This differs from the results for $I_2^-(Ar)_{12,16}$, for which solvent evaporation from the $\tilde{A}$ state did not appear to be complete by 45–50 ps. Recall, however, that the $\tilde{A}$ state parameters were determined by setting $\langle n_A \rangle$ in the 3 ns spectrum of $I_2^-(Ar)_{20}$ equal to the photofragmentation value (see Analysis), so agreement at the longest times between $\langle n_A \rangle$ at long time delays (11.0 ± 0.5) and the photofragmentation average (11.1) is guaranteed. Nonetheless, $\langle n_A \rangle$ has reached this asymptotic value by 15 ps.

It seems unusual that solvent evaporation from $\tilde{A}$ state recombination and relaxation should be complete by 15 ps from $I_2^-(Ar)_{20}$ but incomplete by 50 ps in the smaller clusters $I_2^-(Ar)_{12,16}$. A possible explanation is that our assumption of complete evaporation by 3 ns from $I_2^-(Ar)_{20}$ is incorrect, so that from 15 ps to 3 ns the number of solvent atoms is constant and higher than the photofragment value, with complete evaporation only at longer times. This implies solvent evaporation from the $\tilde{A}$ state is even slower than in the simulations of Faeder *et al.*[28] for $I_2^-(Ar)_{20}$, which predict a slow but steady evaporation of Ar atoms after 10–20 ps. As a result, their simulated photoelectron spectra for the $\tilde{A}$ state feature shifts toward higher eKE from 20 to 200 ps, in contrast to the experimental FPE spectra which show no such shift. It appears that that more work is required on I_2^- ($\tilde{A}$) and its interactions with the solvent, since the well depth of this state is only a factor of 3 larger than the $Ar \cdot I^-$ binding energy.

We now consider dynamics in the $\tilde{X}$ state in more detail. The average vibrational level $\langle v \rangle$ of the $\tilde{X}$ state and the average number of solvent atoms $\langle n_X \rangle$ obtained from our FPES simulations are plotted vs time in Figs. 9(a) and 9(b), along with the same quantities from the MD simulations of Faeder *et al.*[28] Between 6.0 ps and 3 ns, the FPES $\langle v \rangle$ drops from 40.0 to 5.1, with most of the decrease occurring before 50 ps. There is little difference in $\langle v \rangle$ between 200 ps and 3 ns, as expected since solvent evaporation is virtually complete by 200 ps. The Faeder *et al.* results have been adjusted to reflect the available energy from a 780 nm photon, rather than 790 nm as used in their study. The time scale for vibrational relaxation in the Faeder *et al.* results is similar, and while there is a sizable discrepancy between 6.0 and 35 ps, the curves match fairly well at later time delays.

In the FPES data, $\langle n_X \rangle$ drops from 8.0 to 0.0 between 6.0 ps and 3 ns, with the majority of the Ar loss (6.0) occurring before 50 ps. The final ~2.0 Ar atoms take longer than 150 ps to evaporate, consistent with the slowdown in evaporation rates seen in other clusters. The Faeder *et al.* data display excellent agreement with the experiment at time delays $\geqslant$6 ps. The agreement is encouraging, for it not only suggests that the model is correctly describing the mechanism of vibrational relaxation and solvent evaporation, but also that our method of determining $\langle n_X \rangle$ is valid.

From Figs. 9(a) and 9(b), one can determine how vibrational relaxation and solvent evaporation track one another. We define E_{solv}, the total solvent energy that can be removed by evaporation of Ar atoms, as

$$E_{\text{solv}} = \langle n_X \rangle \Delta E_{\text{evap}}, \tag{2}$$

where ΔE_{evap} is the average energy lost from the cluster by evaporation of one Ar atom (73 meV).[7] E_{int}, the average I_2^- internal energy in excess of the final (3 ns FPES) energy, is obtained by

$$E_{\text{int}} = E(\langle v \rangle) - E(\langle v \rangle)_f, \tag{3}$$

where $E(\langle v \rangle)$ is the Morse energy for vibrational level $\langle v \rangle$, and $\langle v \rangle_f (=5.1)$ is the average vibrational level at 3 ns.

Subtracting E_{int} from E_{solv}, one obtains a positive excess ''cluster'' energy E_{cluster}, representing the energy stored in the Ar solvent atoms remaining in the cluster. E_{cluster} is plotted vs time in Fig. 9(c), along with the same quantity calculated using the data from Faeder *et al.*[28] (adjusted for 780 nm, and assuming $\langle v \rangle_f$ is equal to the FPES value). Both plots show a general decrease with time. The experimental E_{cluster} drops from 180 meV at 6.0 ps to 0 by 3 ns. The MD simulations show higher values at all time delays, particularly at earlier times (320 meV at 6.0 ps), the disparity being due to the smaller $\langle v \rangle$ relative to the experimental data at these time delays.

The excess cluster energy (at 6.0 ps, equivalent to 2.5 extra Ar atoms in the experimental data, and 4.4 atoms in the simulation) implies that energy is temporarily tied up in solvent modes after removal from the I_2^- vibrational coordinate, but before solvent evaporation. The amount of excess energy is expected to be larger at early times, because there are more solvent atoms available to provide for storage of this energy. For solvent molecules with a stronger binding energy to I_2^- (such as CO_2), this storage capacity is larger, allowing greater amounts of energy to be stored for longer times.[35] Although there is disagreement between the MD simulations and the FPES data in $\langle v \rangle$, which in turn affects E_{cluster}, the signature of a delayed evaporation mechanism is undeniable in both model and experiment.

VI. CONCLUSIONS

FPES has been used to study the photodissociation, recombination and energy transfer dynamics of $I_2^-(Ar)_n$ clusters over a range of sizes. The results show how dynamics evolve with size in these clusters and allow for detailed comparison with theory. Analysis of the FPE spectra yields the

extent of solvation of I^- and I_2^- at each delay time, along with the electronic state and vibrational distribution of the I_2^-. From determination of the number of Ar atoms surrounding the nascent I^- product, the anomalous charge-switching nature of the $\tilde{A}'$ state is confirmed, with the electron localized on the less-solvated I atom immediately after photoexcitation. Subsequent separation of I^- and I fragments results in a decreasing number of Ar atoms through ~1.5 ps in all clusters, after which the dissociated products have been formed in the case of small ($n=6$) clusters, or recombination on the I_2^- $\tilde{X}$ or $\tilde{A}$ states begins to occur in larger ($n \geqslant 12$) clusters.

In $I_2^-(Ar)_{12}$ and $I_2^-(Ar)_{16}$, vibrational relaxation in the $\tilde{X}$ state was slight or unobservable, and the final vibrational level remained quite high ($\langle v \rangle = 68$ and 34, respectively). In $I_2^-(Ar)_{20}$, however, extensive vibrational relaxation was observed, accompanied by evaporation of solvent. Maximum relaxation (to $\langle v \rangle = 5.1$) is achieved by 3 ns, with the loss of all Ar atoms. The average vibrational level $\langle v \rangle$ and number of solvent atoms $\langle n_X \rangle$ were compared to the theoretical study of Faeder *et al.*,[28] which agreed in large measure, despite a discrepancy in $\langle v \rangle$ between 6.0 and 35 ps. Further analysis revealed excess energy stored in the cluster, demonstrating a delay between removal of I_2^- vibrational energy to the cluster, and its dissipation through solvent evaporation, in both the experimental and theoretical studies.

Simulations of the FPE spectra show that significant recombination of I_2^- on the $\tilde{A}$ state occurs for $I_2^-(Ar)_{12}$, $I_2^-(Ar)_{16}$, and $I_2^-(Ar)_{20}$. Although I_2^- $\tilde{X}$ state solvent evaporation is complete on the time scale of the experiment, evaporation resulting from recombination on the I_2^- $\tilde{A}$ state appears to be considerably slower, in qualitative agreement with MD simulations. A comparison of the three clusters suggests that evaporation resulting from $\tilde{A}$ state recombination in $I_2^-(Ar)_{20}$ may not be complete by 3 ns, in disagreement with MD simulations. Dynamics on the $\tilde{A}$ state are likely to be very sensitive to its well depth and equilibrium internuclear separation, neither of which has been spectroscopically determined. A more accurate characterization of this state, perhaps using a method recently applied to the $\tilde{A}'$ state,[44] would be highly desirable.

ACKNOWLEDGMENTS

This research is supported by the National Science Foundation under Grant No. CHE-9710243. Equipment support from the Defense University Research Instrumentation Program under Grant No. F49620-95-1-0078 is also gratefully acknowledged. The authors would like to thank James Faeder, Nicole Delaney, Robert Parson, and Victor Batista for many helpful discussions.

[1] M. L. Alexander, N. E. Levinger, M. A. Johnson, D. Ray, and W. C. Lineberger, J. Chem. Phys. **88**, 6200 (1988).
[2] J. M. Papanikolas, J. R. Gord, N. E. Levinger, D. Ray, V. Vorsa, and W. C. Lineberger, J. Phys. Chem. **95**, 8028 (1991).
[3] M. E. Nadal, P. D. Kleiber, and W. C. Lineberger, J. Chem. Phys. **105**, 504 (1996).
[4] S. Nandi, A. Sanov, N. Delaney, J. Faeder, R. Parson, and W. C. Lineberger, J. Phys. Chem. A **102**, 8827 (1998).
[5] A. Sanov, S. Nandi, and W. C. Lineberger, J. Chem. Phys. **108**, 5155 (1998).
[6] V. Vorsa, Ph.D. thesis, University of Colorado, Boulder, 1996.
[7] V. Vorsa, P. J. Campagnola, S. Nandi, M. Larsson, and W. C. Lineberger, J. Chem. Phys. **105**, 2298 (1996).
[8] D. Ray, N. E. Levinger, J. M. Papanikolas, and W. C. Lineberger, J. Chem. Phys. **91**, 6533 (1989).
[9] J. M. Papanikolas, V. Vorsa, M. E. Nadal, P. J. Campagnola, J. R. Gord, and W. C. Lineberger, J. Chem. Phys. **97**, 7002 (1992).
[10] J. M. Papanikolas, V. Vorsa, M. E. Nadal, P. J. Campagnola, H. K. Buchenau, and W. C. Lineberger, J. Chem. Phys. **99**, 8733 (1993).
[11] V. Vorsa, S. Nandi, P. J. Campagnola, M. Larsson, and W. C. Lineberger, J. Chem. Phys. **106**, 1402 (1997).
[12] B. J. Greenblatt, M. T. Zanni, and D. M. Neumark, Science **276**, 1675 (1997).
[13] B. J. Greenblatt, M. T. Zanni, and D. M. Neumark, Faraday Discuss. **108**, 101 (1997).
[14] A. E. Johnson, N. E. Levinger, and P. F. Barbara, J. Phys. Chem. **96**, 7841 (1992).
[15] D. A. V. Kliner, J. C. Alfano, and P. F. Barbara, J. Chem. Phys. **98**, 5375 (1993).
[16] J. C. Alfano, Y. Kimura, P. K. Walhout, and P. F. Barbara, Chem. Phys. **175**, 147 (1993).
[17] I. Benjamin, P. F. Barbara, B. J. Gertner, and J. T. Hynes, J. Phys. Chem. **99**, 7557 (1995).
[18] P. K. Walhout, J. C. Alfano, K. A. M. Thakur, and P. F. Barbara, J. Phys. Chem. **99**, 7568 (1995).
[19] L. Perera and F. G. Amar, J. Chem. Phys. **90**, 7354 (1989).
[20] F. G. Amar and L. Perera, Z. Phys. D **20**, 173 (1991).
[21] P. E. Maslen, J. M. Papanikolas, J. Faeder, R. Parson, and S. V. ONeil, J. Chem. Phys. **101**, 5731 (1994).
[22] J. M. Papanikolas, P. E. Maslen, and R. Parson, J. Chem. Phys. **102**, 2452 (1995).
[23] P. E. Maslen, J. Faeder, and R. Parson, Chem. Phys. Lett. **263**, 63 (1996).
[24] V. S. Batista and D. F. Coker, J. Chem. Phys. **106**, 7102 (1997).
[25] J. Faeder, N. Delaney, P. E. Maslen, and R. Parson, Chem. Phys. Lett. **270**, 196 (1997).
[26] N. Delaney, J. Faeder, P. E. Maslen, and R. Parson, J. Phys. Chem. A **101**, 8147 (1997).
[27] B. M. Ladanyi and R. Parson, J. Chem. Phys. **107**, 9326 (1997).
[28] J. Faeder and R. Parson, J. Chem. Phys. **108**, 3909 (1998).
[29] P. E. Maslen, J. Faeder, and R. Parson, Mol. Phys. **94**, 693 (1998).
[30] J. Faeder, N. Delaney, P. E. Maslen, and R. Parson, Chem. Phys. **239**, 525 (1998).
[31] N. Delaney, J. Faeder, and R. Parson, J. Chem. Phys. **111,** 452 (1999).
[32] C. J. Margulis and D. F. Coker, J. Chem. Phys. **110**, 5677 (1999).
[33] B. J. Greenblatt, M. T. Zanni, and D. M. Neumark, Chem. Phys. Lett. **258**, 523 (1996).
[34] M. T. Zanni, T. R. Taylor, B. J. Greenblatt, B. Soep, and D. M. Neumark, J. Chem. Phys. **107**, 7613 (1997).
[35] B. J. Greenblatt, M. T. Zanni, and D. M. Neumark, J. Chem. Phys. (in press).
[36] V. S. Batista and D. F. Coker, J. Chem. Phys. **106**, 6923 (1997).
[37] M. T. Zanni, B. J. Greenblatt, and D. M. Neumark, J. Chem. Phys. **109**, 9648 (1998).
[38] K. Asmis, T. Taylor, and D. M. Neumark, J. Chem. Phys. **109**, 4389 (1998).
[39] V. S. Batista and D. F. Coker, J. Chem. Phys. **110**, 6583 (1999).
[40] W. C. Wiley and I. H. McLaren, Rev. Sci. Instrum. **26**, 1150 (1955).
[41] O. Cheshnovsky, S. H. Yang, C. L. Pettiette, M. J. Craycraft, and R. E. Smalley, Rev. Sci. Instrum. **58**, 2131 (1987).
[42] L.-S. Wang, H.-S. Cheng, and J. Fan, J. Chem. Phys. **102**, 9480 (1995).
[43] B. J. Greenblatt, Ph.D. thesis, University of California, 1999.
[44] M. T. Zanni, V. S. Batista, B. J. Greenblatt, W. H. Miller, and D. M. Neumark, J. Chem. Phys. **110**, 3748 (1999).
[45] C. E. Moore, *Atomic Energy Levels*, NSRDS-NBS 35 (U.S. GPO, Washington, D.C., 1971), Vol. 1.
[46] I. Yourshaw, Y. Zhao, and D. M. Neumark, J. Chem. Phys. **105**, 351 (1996).
[47] T. Kuhne and P. Vohringer, J. Chem. Phys. **105**, 10788 (1996).
[48] S. E. Bradforth, Ph.D. thesis, University of California, Berkeley, 1992.
[49] N. Delaney, J. Faeder, and R. Parson (private communication).